Ionospheric and Magnetospheric Responses to the Extreme Geomagnetic Storm of May 10–12, 2024

Tesfau Hagos Tadesse[1], Gebiregiorgis Abraha Fikade[2*] and Yikdem Mengesha Gebrehiwot[3]

[1]Department of Physics, College of Natural and Computational Sciences, Mekelle University, Mekelle, Tigray, Ethiopia (tesfulidya25@gmail.com; https://orcid.org/0009-0005-2849-3032).

[2]Department of Physics, College of Natural and Computational Sciences, Mekelle University, Mekelle, Tigray, Ethiopia (*ggabraha@gmail.com; https://orcid.org/0009-0004-6478-6636).

[3]Department of Physics, College of Natural and Computational Sciences, Mekelle University, Mekelle, Tigray, Ethiopia (yikdem.mengesha@mu.edu.et; https://orcid.org/0000-0003-4907-1726).

ABSTRACT

This paper investigates the global ionospheric and magnetospheric responses to the extreme solar-driven superstorm of May 10–12, 2024. Special focus is placed on the spatiotemporal evolution of storm-enhanced density (SED) plumes, mid-latitude ionospheric troughs, and the intensification of the Equatorial Ionization Anomaly (EIA). Utilizing a multi-instrument framework, we integrate ground-based GNSS observations from IGS networks with in-situ topside plasma measurements from the ESA Swarm satellite constellation. The dates May 10-12, 2024 were specifically selected because they correspond to the occurrence of one of the most intense and historically significant geomagnetic storms of solar cycle 25 according to NOAA. The extreme solar conditions generated strong Magnetosphere-Ionosphere coupling processes, leading to substantial ionospheric disturbances. The results reveal severe, widespread upper-atmospheric disruptions during the storm's main phase. Peak Total Electron Content (TEC) values exceeded 200 TECU, while the Rate of TEC Index (ROTI) and amplitude scintillation (S_4) index surpassed 0.8 TECU/min and 0.9, respectively. The EIA exhibited an intensely enhanced positive storm phase characterized by a profound poleward expansion of the crests. This expansion was driven by a combination of prompt penetration electric fields (PPEFs) and disturbed equatorward thermospheric winds that uplifted the F-layer plasma via enhanced ExB drift. Concurrently, high-rate S_4 index measurements captured strong nighttime localized irregularities generated by the rapid growth of plasma bubbles and auroral precipitation. During the recovery phase, mid-latitude regions transitioned into a long-lasting negative ionospheric storm phase, mediated by enhanced chemical recombination and plasma redistribution. These findings characterize the structural dynamics of superstorms during Solar Cycle 25 and provide critical observational constraints for mitigating space weather hazards on global navigation satellite systems (GNSS) and satellite communications. One of our findings shows that, unlike typical geomagnetic storms, an explicit Storm Sudden Commencement (SSC) was apparent during this event.

Keywords: TEC, Superstorm Geomagnetic Event, Ram Pressure, Dst Index, CME.

1. INTRODUCTION

Extreme geomagnetic storms, which are intense disturbances in Earth's magnetic field caused by solar eruptions such as coronal mass ejections (CMEs) and solar flares, can cause drastic changes in the ionosphere's electron density (Gopalswamy, 2009). These storms disrupt satellite-based

Momona Ethiopian Journal of Science (MEJS), V18(2):290-310,2026 ©CNCS, Mekelle University, ISSN:2220-184X

Submitted: 23rd November 2025 Accepted: 26th August 2026 Published: 29th October 2026

© CNCS Mekelle University. This article is licensed under a Creative Commons Attribution 4.0 International License. This license enables re-users to distribute, remix, adapt, and build upon the material in any medium or format, so long as attribution is given to the creator. The license allows for commercial use. To view the details of this license, visit http:// creativecommons.org/ licenses/ by/4. 0/. CC: Creative Commons; BY: credit must be given to the creator.

communication, navigation, and power grids, making it essential to understand how the ionosphere responds to such events. The 25th solar cycle, which began in December 2019, marks the rising phase of solar activity characterized by increasing sunspot numbers, solar flares, and geomagnetic storms (Feng et al., 2023). This phase provides a valuable opportunity to study the ionospheric response to extreme geomagnetic storms. Understanding the ionospheric behavior during such periods is crucial, especially for mitigating the adverse effects of space weather on modern technological systems such as (GNSS), which rely heavily on stable ionospheric conditions. Ionospheric Response to Geomagnetic Storms is triggered when solar wind disturbances compress Earth's magnetosphere, generating strong currents in the ionosphere, referred to as auroral electrojet (Wan et al., 2021).

The response of the ionosphere to these storms typically follows a complex sequence of positive and negative phase changes. In the positive phase, TEC increases due to enhanced ionization caused by energetic particles, while in the negative phase, TEC decreases due to disturbed ionospheric composition and reduced solar radiation (Maruyama & Nakamura, 2007). During the Halloween super storm from October 30 - 31, 2003, the observed anomalies reached ~30^{o} magnetic latitudes, while the May 10-12, 2024 anomalies reached ±45^{o} magnetic latitudes (Hajra et al., 2024).

Numerous studies such as (Lin et al., 2005; Matsushita, 1959), have examined ionospheric responses during previous solar cycles, particularly in relation to strong geomagnetic storms. For instance, during the 24th solar cycle, geomagnetic storms were found to cause widespread TEC enhancements at equatorial and mid-latitudes, while high latitude regions often experienced TEC depletion (Jakowski et al., 1999). These variations are influenced by factors such as the intensity of solar wind, seasonal conditions, geomagnetic latitude, and local time (Lin et al., 2005). Ionospheric storms contain positive and negative phases, which are defined by the enhancement/depletion in electron density, respectively, according to the quiet time values (Bauske and Prölss, 1998). The electron density of an ionosphere depends on the storm time, storm magnitude, event location, season, and solar activity level (Matsushita, 1959). On a global and local scale, the storm-time TEC response during an ionospheric storm was investigated by many researchers using GNSS data, which provides low cost, continuous, abundant, high-quality, high-rate temporal and high resolution spatial ionospheric data (Jakowski et al., 1999; Baran et al., 2001; Yin et al., 2004; Blagoveshchensky et al., 2018; Sharma et al., 2020). Global TEC response during

the severe magnetic storm on June 22-23, 2015, was investigated using GNSS-based TEC data from GIMs, COSMIC RO, and a chain of IGS stations.

These missions allow for detailed tracking of storm-induced TEC disturbances, including the formation of ionospheric irregularities, plasma bubbles, and scintillation events that affect GNSS signal stability (Imam et al., 2024). Preliminary data from recent storms during the 25th solar cycle indicate significant storm-time enhancements in TEC, particularly in equatorial regions. Additionally, polar ionospheric phenomena in solar cycle 24, such as auroral oval expansion and sub-storm activity, have demonstrated complex effects on TEC and ionospheric current systems (Prikryl et al., 2010). Given the continuous rise in solar activity, further research is necessary to quantify the ionospheric impact of more intense geomagnetic storms expected as the cycle progresses.

To detect ionospheric responses to geomagnetic storms, changes in the TEC of the ionosphere have been examined in recent years (Lin et al., 2005; Jacobsen et al., 2016). Especially, the ionospheric effects of September 7 - 8, 2017 geomagnetic storm caused by the largest solar flare of solar cycle 24, have been investigated by many authors using ionospheric TEC (Zakharenkova et al., 2018; Yuan et al., 2008). In these studies, the ionosphere effects of the geomagnetic storm where generally considered as regional. The effects of storm on September 7 - 8, 2017 are globally investigated by the Rate of Total Electron Content (TEC) Index (ROTI) suggested by Liu et al. (2020); and Pi et al. (1997). Ionospheric delay errors caused by ionospheric storms are very difficult to correct through modeling, and the resulting degradation of the positioning performance of the GNSS is exceptionally strong (Afraimovich et al., 2002; Peng et al., 2021).

Investigations of the ionospheric response to strong geomagnetic storms are mostly developed with case studies (Lin et al., 2005; Dugassa et al., 2023). In particular, the two geomagnetic storms of the 24th solar active cycle (on March 2015 and September 2017) are the most typical. The geomagnetic storm of March 2015, also known as the St. Patrick's Day Storm, was classified as G4 by the National Oceanic and Atmospheric Administration's (NOAA's) space weather classification system. Several studies have investigated the relationship between geomagnetic storms and the ionosphere, as well as their subsequent impacts on GNSS positioning, from various perspectives. For instance, Cherniak and Zakharenkova (2015) utilized data from over 2,500 ground-based GPS receiver stations to demonstrate a strong correlation between high-

latitude ionospheric irregularities and auroral activity during intense geomagnetic storms. At low and middle latitudes, Nava et al. (2016) analyzed ionospheric variations across four geographic sectors (Asia, Africa, the Americas, and the Pacific) and provided physical mechanisms for the observed disturbances. Furthermore, observations from the national real-time kinematic (RTK) positioning network in northern Norway revealed significant ionospheric disturbances; these irregularities were attributed to polar cap plasma patches and particle precipitation driven by magnetic reconnection (Jacobsen et al., 2016; Lanzerotti et al., 2004).

Furthermore, they analyzed RTK and precise point positioning (PPP) performance during the storm. Using GPS and Swarm satellite data, Zakharenkova et al. (2018) identified large-scale plasma irregularities and structured auroral ionospheric regions stretching over 850 km across Russia. The September 2017 coronal mass ejection (CME) and subsequent high-speed solar wind streams triggered a severe geomagnetic storm, generating violent ionospheric disturbances (e.g., Akala et al, 2021**)**. During this event, prompt penetration electric fields (PPEF) induced by the southward IMF Bz significantly enhanced an equatorial plasma bubble (EPB) in the 120°E/60°W longitudinal sector (Li et al., 2018). Additionally, Zhang et al. (2019) have reported simultaneous large and medium-scale TIDs at dusk within sub-auroral and mid-latitude regions. Based on observations from the U.S. Continuously Operating Reference Station (CORS) network, (Jakowski et al., 1999; Liu et al., 2020), explored the TEC of the ionosphere in response to this geomagnetic storm and found medium TIDs with intensities higher than 2.5 TECU. Tariku (2015) discussed nighttime ionospheric behavior during the recovery phase of geomagnetic storms, noting that the nighttime ionosphere in the American sector was largely depressed, while the Asian sector exhibited only a marginal nocturnal TEC increase that was significantly weaker than its daytime counterpart. However, a critical gap remains in understanding whether these longitudinal asymmetries persist, or fundamentally alter, during an "extreme" superstorm (Dst < -400 nT) near the peak of an intense solar maximum. While historical studies focus on moderate-to-severe storms with predictable regional damping, extreme events like the May 10–12, 2024 superstorm present a severe operational problem: the sheer magnitude of electrodynamic coupling can completely override typical longitudinal quiet-time behaviors. There is currently a lack of high-resolution, multi-instrument data addressing how simultaneous plasma bubble growth and extreme auroral boundaries distort nighttime sectors on a global scale. This study addresses this problem directly by evaluating how the unprecedented driving forces of the May 2024 event forced the nightside

ionosphere into anomalies that depart significantly from previously documented storm-recovery baselines.

2. INSTRUMENTATION AND DATA SOURCES

To comprehensively evaluate the ionospheric and magnetospheric responses during the May 2024 event, a multi-source observational dataset was compiled.

2.1. Specific Input Datasets Solar Wind and Interplanetary Drivers

High-resolution (1-minute) IMF Bz , solar wind velocity (V sw), plasma flow pressure, alongside Dst and Kp indices were retrieved from the NASA OMNIWeb database.

2.1.1. Ionospheric Electron Density

Global Ionospheric Maps (GIM) and vertical TEC measurements were derived from the International GNSS Service (IGS) network via Nagoya University.

2.1.2. In-Situ Topside Plasma Parameters

High-resolution in-situ electron density and magnetic field perturbation measurements were collected along the low-Earth orbit (LEO) tracks of the European Space Agency's (ESA) Swarm satellite constellation.

2.1.3. Ionospheric Scintillation Indices

High-rate GNSS scintillation metrics, including the amplitude scintillation (S_4) index and the Rate of TEC Index (ROTI), were retrieved from the Space Weather Services (SWS) World Data Center (https://sws.bom.gov.au/).

2.2. Methodology and Data Analysis

The analysis followed a three-phase cross-validation workflow executed in MATLAB. First, OMNIWeb time-series parameters were extracted to pinpoint the exact onset timings of the Storm Sudden Commencement (SSC), main phase, and recovery phase. Second, ground-based GNSS data were filtered for multipath and elevation cutoffs to map spatial and temporal variations in TEC and calculate ROTI anomalies using a sliding interquartile range method. Third, ground observations were cross-referenced with concurrent Swarm satellite passes to align localized vertical plasma structures, electron density gradients, and scintillation fields. Statistical techniques, including correlation analyses, were then applied to quantify the direct coupling between interplanetary driving forces and the resulting low-, mid-, and high-latitude ionospheric anomalies.

3. RESULTS AND DISCUSSION

3.1. Characterization of the Geomagnetic Storm event of May 10-12/2024

The extreme geomagnetic storm of May 10–12, 2024, stands out as one of the most intense space weather events of Solar Cycle 25. Figure (1a) displays the synchronized variations of the IMF parameters (Bx, By, Bz), solar wind velocity (Vsw) figure (1c), Kp index figure(1e), the eastward electric field figure(1b), plasma flow pressure figure(1d), and Dst index figure (1f).

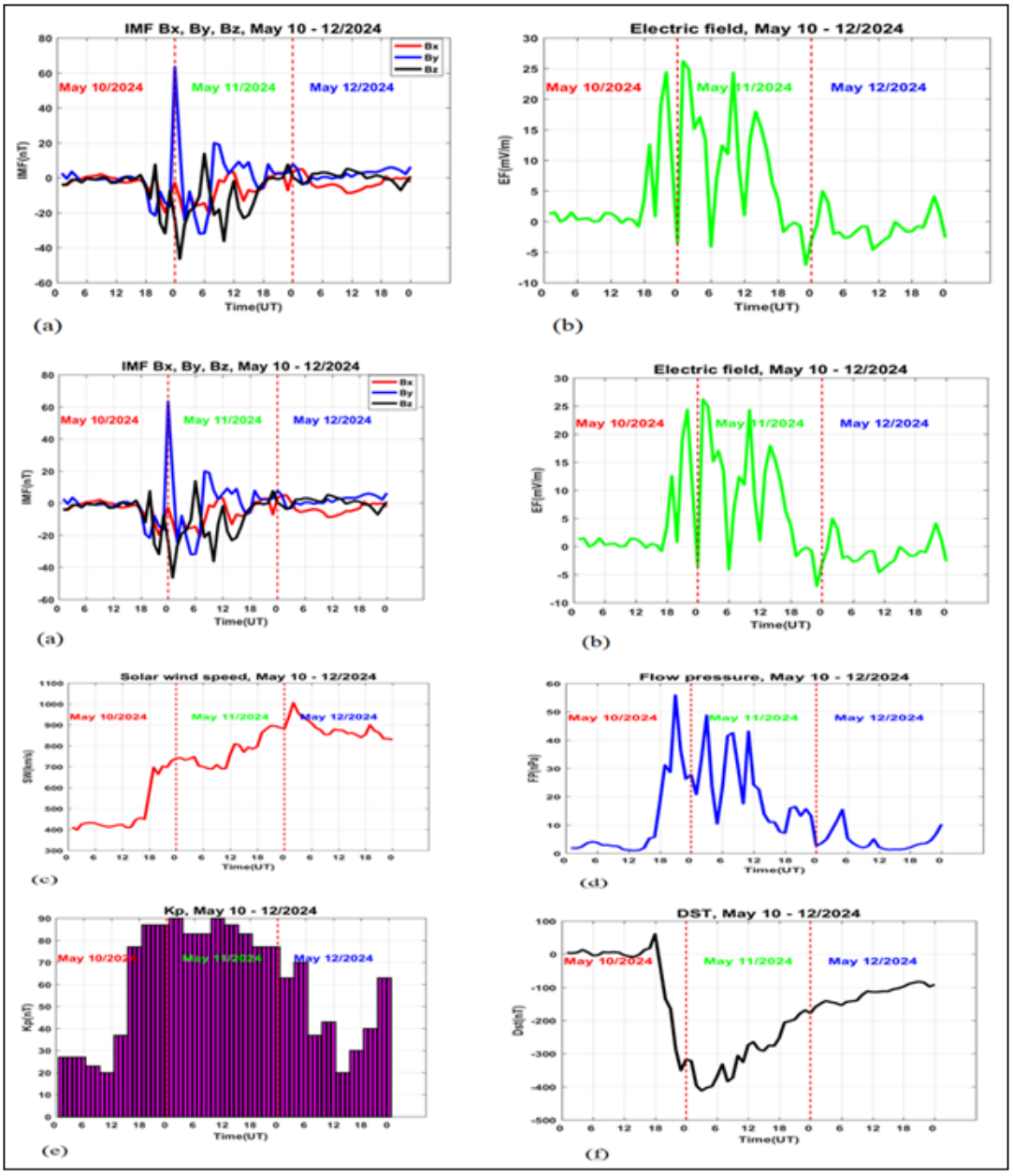


Figure 1. Graphs of solar wind parameters: (a) IMF Bx, By, Bz, (b) electric field, (c) solar wind, (d) flow pressure, (e) Kp index, and (f) Dst index.

Prior to 18:00 UT on May 10, the IMF components and electric field remained calm and stable. Following the initial impact of a dense coronal mass ejection (CME), an explicit Storm Sudden Commencement (SSC) occurred, forcing the Dst index to briefly spike to 35 – 61 nT between 12:00 and 17:00 UT. Concurrently, the solar wind speed rapidly accelerated past 702–742 km/s, driving the interplanetary ram pressure to an exceptional peak of 55.89 nPa by 20:00 UT. This extreme compression of the dayside magnetosphere increased reconnection rates, causing the IMF Bz component to plunge sharply southward to a minimum of -46.5 nT by 00:00–01:00 UT on May 11. Driven by these intense Prompt Penetration Electric Fields (PPEFs), the eastward electric field fluctuated sharply, increasing from baseline quiet-time levels up to 24.39 mV/m at 21:00 UT and peaking at 26.16 mV/m at 00:00 UT during the storm's main phase. These electrodynamic forces induced rapid plasma redistribution and enhanced the equatorial ionization fountain effect. Consequently, the planetary Kp index maximized at 9, and the Dst index dropped precipitously to a peak negative intensity of -412 nT at 02:00 UT on May 11, establishing this event as an historic solar cycle superstorm followed by a prolonged recovery phase.

These fluctuations are directly linked to changes in the magnetospheric connection pattern and the interaction between the solar wind and Earth's magnetosphere which is consistent with the results reported by Hajra et al. (2024). Unlike typical geomagnetic storms (Gonzalez et al., 1994), an explicit Storm Sudden Commencement (SSC) was apparent during this event.

3.2. Ionospheric Response to Geomagnetic Storm: Spatial and Temporal TEC Variation

The extreme solar wind driving forces scaled up the auroral electrojets and accelerated particle precipitation into the lower thermosphere, exponentially driving up local electron density and manifesting as prominent positive ionospheric TEC anomalies at mid- and high-latitudes during the storm's main phase. Simultaneously, the severe intensification and expansion of the Equatorial Ionization Anomaly (EIA) triggered extreme positive anomalies, mediated by PPEFs and disturbed neutral winds that uplifted the ionospheric F-layer via enhanced ExB drift. This mechanism forced the EIA crests to expand poleward up to $\pm 45^0$ magnetic latitudes representing a major departure from standard solar-maximum behaviors where crests remain confined within $\pm 15^0 - 20^0$. Conversely, during the recovery phase, mid-latitude regions transitioned into pronounced negative TEC anomalies driven by an increased neutral N_2/O ratio that accelerated chemical recombination.

To evaluate these global dynamics, hourly averaged Global Ionospheric Maps (GIMs) and anomalies were tracked across different latitudinal zones via the Madrigal database. On May 10,

as seen in figure 2, the ionosphere remained normal before 18:00 UT, displaying typical dual equatorial crest lines. After 18:00 UT, storm-time electrodynamic anomalies emerged: the geomagnetic equator weakened as plasma was evacuated poleward, causing the EIA crests to swell past 200 TECU at 85^0 W longitudes. By 22:00 UT, the EIA intensity maximized, exceeding quiet-day baselines by (>200 TECU). Localized peak clusters exceeding 200 TECU encompassed the tropical Eastern Pacific, Southern Asia, and the Australian sectors. Because these sectors crossed the day-to-dusk window during the main phase, intense PPEFs amplified the upward fountain effect, while storm-driven equatorward neutral winds pushed the plasma to high, low-recombination F-layer altitudes.

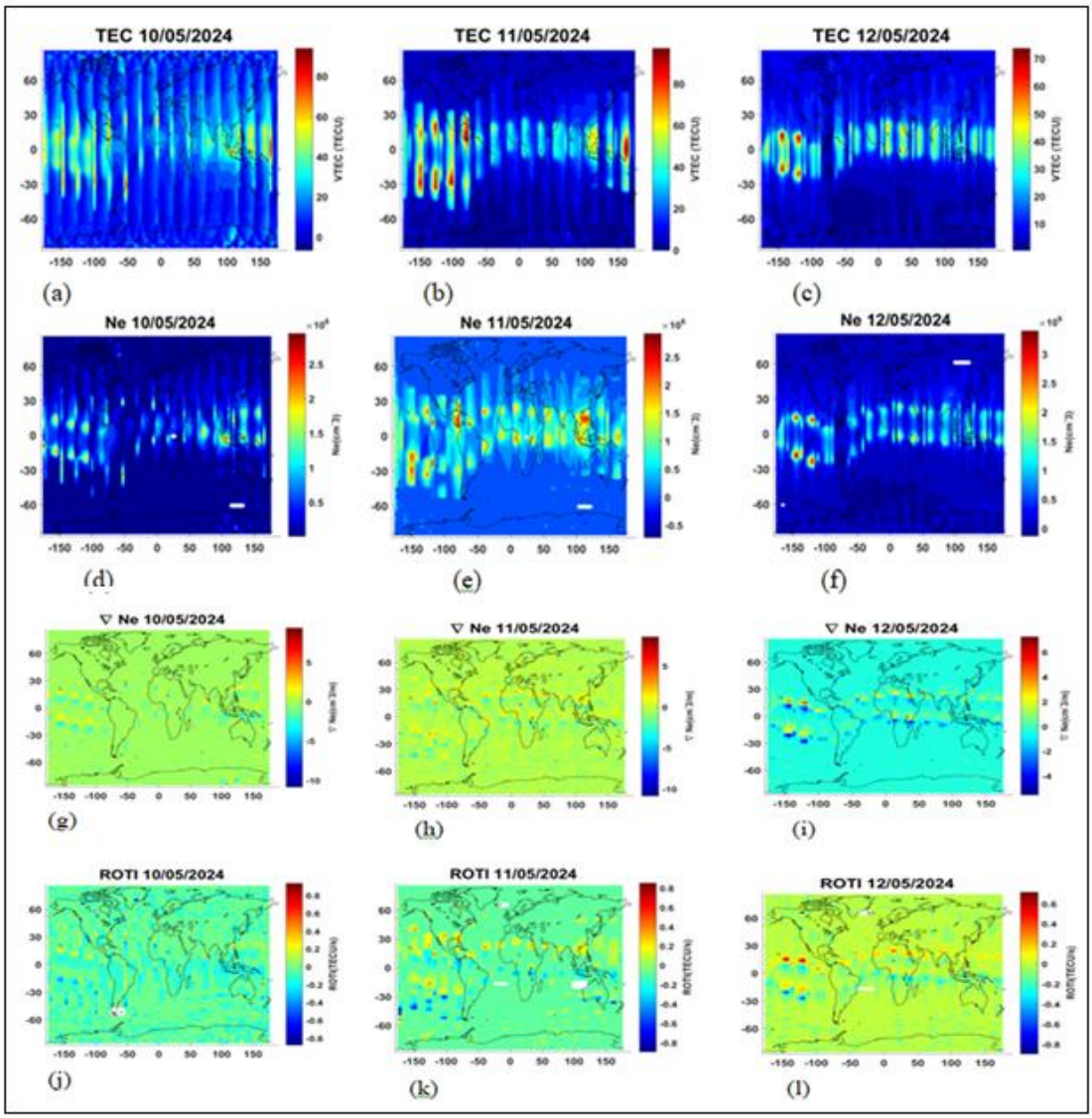


Figure 2. Global ionospheric TEC maps for 10 May 2024, shown in 2-hour UT averages to illustrate diurnal evolution.

On May 11 as seen in figure 3 at 00:00 UT, global ionospheric TEC peaked at 150 TECU, maximizing between 10^0 N and 30^0 N over North America, with elevated values matching the mid-latitude EIA crest zones across South America. By 02:00 UT, the peak value decreased to 100 TECU. Between 02:00 UT and 10:00 UT, peak values fluctuated between 100 and 110 TECU, before dropping to 60 TECU between 12:00 and 14:00 UT due to enhanced recombination and storm-time neutral wind dampening. Although a secondary increase reached 90 TECU between 16:00 and 22:00 UT, the overall electron content near the EIA crests over the Americas did not show further substantial expansion.

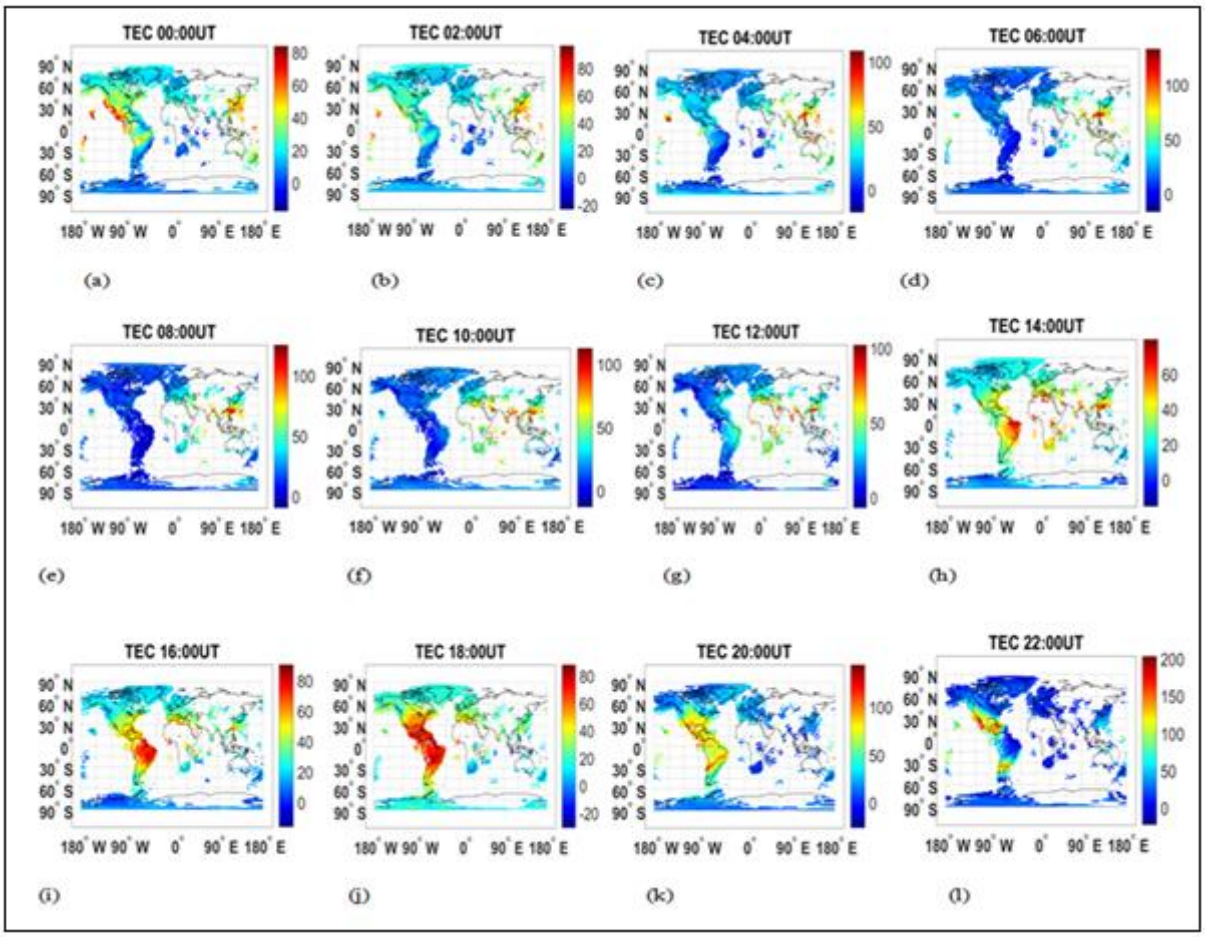


Figure 3. Global ionospheric TEC maps for 11 May 2024, shown in 2-hour UT averages to illustrate diurnal evolution.

On May 12, as shown in figure 4 the ionosphere entered a fluctuating recovery phase: values sat at 100 TECU at 00:00–02:00 UT 180^0 W), shifted to 120 TECU between 04:00 and 08:00 UT 180^0 E and peaked at 160 TECU at 12:00 UT over East Africa and the Indian Ocean before gradually declining back to a stable 100 TECU threshold by the end of the day.

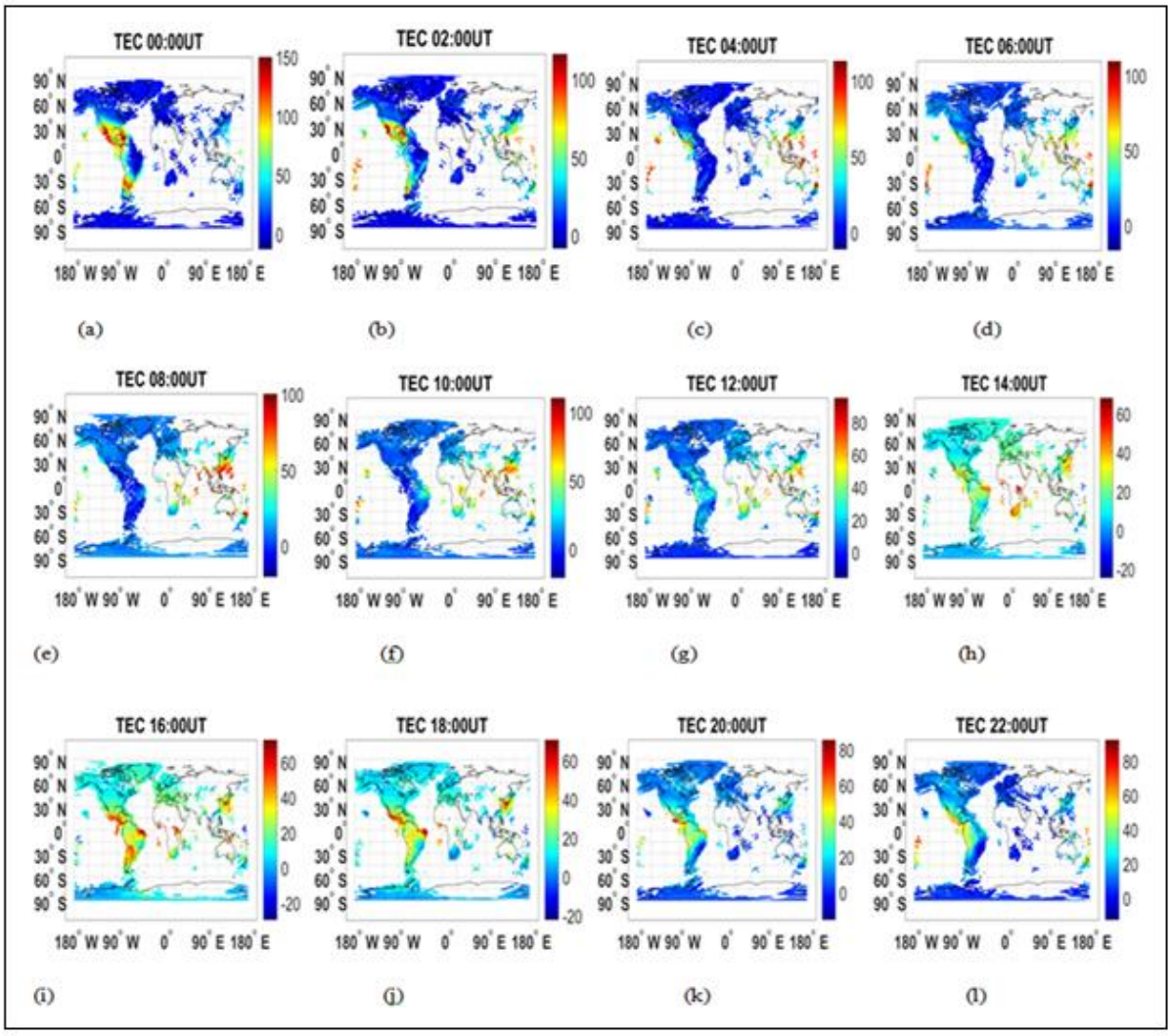


Figure 4. Global ionospheric TEC maps for 12 May 2024, shown in 2-hour UT averages to illustrate diurnal evolution.

3.3. Ionospheric Irregularities and LEO Satellite Cross-Validation

The spatiotemporal distribution of macroscopic ionospheric irregularities was cross-validated using ground-based metrics alongside in-situ data from the ESA Swarm satellite constellation. On May 10, the daily TEC profile derived from Swarm reached a maximum of 90 TECU along the northern peak of the EIA (150^0 W and 120^0 E). During the extreme geomagnetic storm phase on May 11, the peak electron density (Ne) initially increased to 2.9×10^6 cm^{-3} over low-latitude sectors before gradually dropping to 2.5×10^6 cm^{-3} as the main phase gave way to localized mid-latitude enhancements (3.4×10^6 cm^{-3} over the Pacific Ocean on May 12). During the main phase, the TEC exhibited significant fluctuations. Energy injection from the solar wind can cause enhanced

ionization and increased TEC values, especially at high and mid-latitudes due to aurora electro jet currents and energetic particle precipitation (Astafyeva et al., 2020**)**.

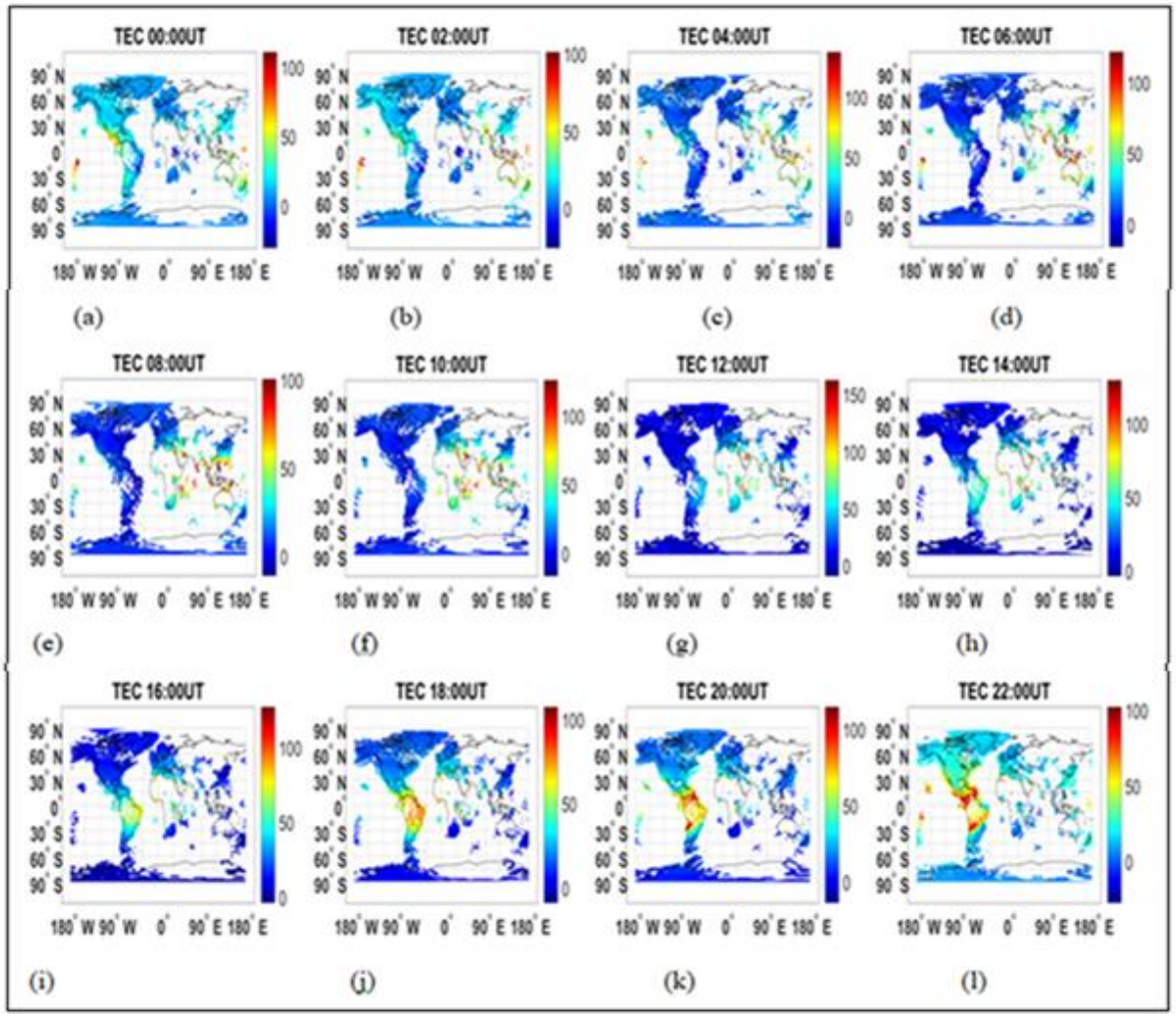


Figure 5. Distribution of hours-averaged values of global ionospheric TEC, Electron density, Electron density gradient, and ROTI from 10 - 12, May 2024.

The rate of TEC Index (ROTI) and electron density gradient (∇Ne) profiles as seen in figure 5 reveal severe plasma turbulences. On May 10, elevated ROTI values (>0.6 TECU/min) were observed across the northern sectors of North America and Africa. On May 11, under peak geomagnetic driving, ROTI values surpassed 0.8 TECU/min over central North America and northern Africa, while expanding across central South America, southern Africa, and Australia. Simultaneously, the maximum ∇Ne steepened dramatically from a pre-storm value of 2.5 to a maximum storm-time value of 8 around the EIA crests, North America, North Africa, and India. This steepening indicates the generation of severe equatorial plasma bubbles (EPBs) and high-

latitude plasma patches triggered by enhanced electric fields and disrupted ionospheric current distributions.

During geomagnetic storms, the electron density gradient around low latitudes can exhibit both high and low values due to the complex and dynamic responses of the ionosphere to storm induced disturbances. Geomagnetic storms enhance the electric fields and ionospheric currents, disrupting the usual patterns of electron density distribution, especially around the EIA. The storm-induced electric fields can intensify the equatorial fountain effect, which enhances plasma uplift and pushes more electrons into the EIA crests, resulting in steeper gradients in those regions. Conversely, storm-time changes can also cause ionospheric depletion, leading to lower electron densities in other parts of the low-latitude ionosphere, particularly closer to the equator. We investigated the variation of TEC globally from GPS and GNSS observations.

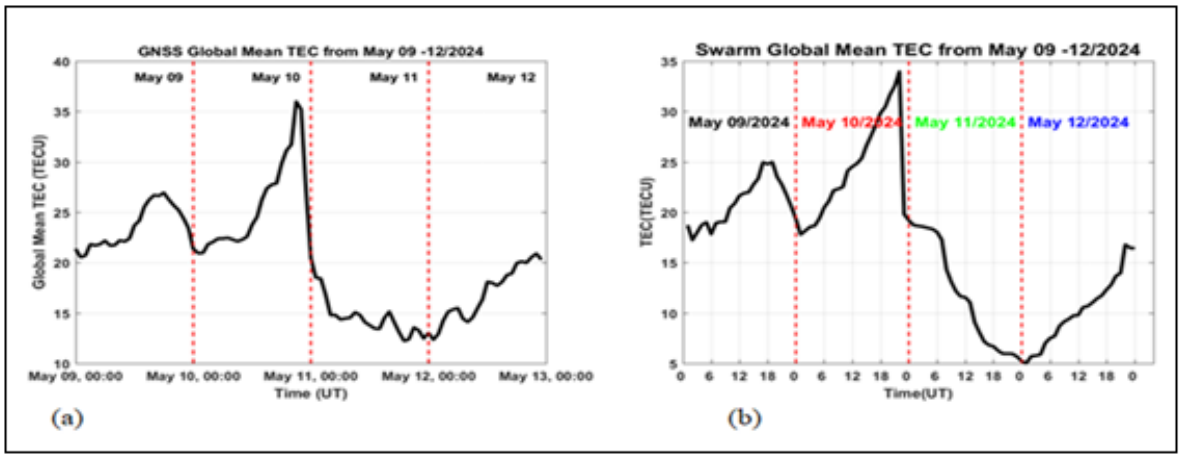


Figure 6. Global mean TEC versus time of GNSS left panel and Swarm right panel for May 9-12, 2024.

Figure 6 displays the global mean TEC in TECU over four days (May 9-12, 2024). On May 9, 2024 the TEC values remained relatively stable fluctuating between 20 - 25 TECU. This indicates a normal state of the ionosphere prior to the geomagnetic storm. During the main phase May 10 TEC showed rapid increase, reaching a peak value of approximately 35-38 TECU. This surge is the characteristic of the ionospheric response to increased solar activity. During the geomagnetic storm, energy input from magnetosphere enhances ionization level in the ionosphere, leading to elevated TEC. In the storm recovery phase (May 11-12, 2024) the TEC sharply decreased after the peak, dropping below 15 TECU by early May. This sudden reduction indicates depletion of ionospheric plasma, potentially due to enhanced recombination rates or redistribution of plasma driven by geomagnetic disturbances. On May 11 and May 12, TEC values exhibited

gradual recovery but remained below the pre- storm levels. The physical mechanism for the recovery is the dissipation of storm time energy and stabilization of the geomagnetic field allowed ionospheric electron densities to re-establish equilibrium.

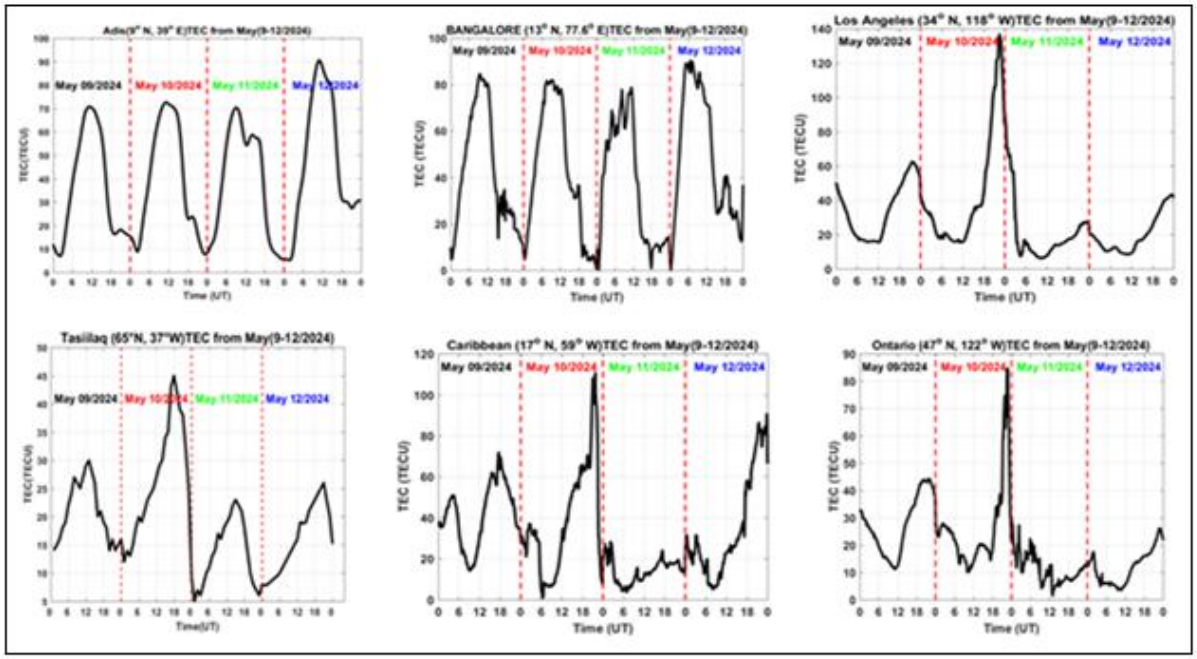


Figure 7. Spatiotemporal variations of Total Electron Content (TEC) across different latitudes from May 9 to 12, 2024.

Figure 7 shows the response of the ionosphere to geomagnetic storm by analyzing TEC variations at three distinct geographic regions. During pre-storm time, the equatorial region (15^0 N, 59^0 W) shows highest TEC values due to the equatorial ionization anomaly (EIA). In quiet condition, electric fields and neutral winds push plasma away from the magnetic equator to regions $15 – 20^0$ north and south, enhancing TEC near these latitudes. TEC values at mid latitude (47^0 N, 112^0 W) are moderate and exhibit a weaker diurnal trend compared to the equatorial region. The ionization here is controlled by solar zenith angle and atmospheric composition. The TEC values at high latitude (65^0 N, 37^0 W), however, are lowest because of the reduced solar radiation and geomagnetic effect that limit ionospheric density. During storm sudden commencement (May 10), the onset of the geomagnetic storm significantly impacts the ionosphere, with the largest TEC peak (> 110 TECU), particularly in the equatorial region. This may be caused by storm time penetration electric fields, thermospheric expansion and winds, and super fountain effect. The mid latitude region became greater than the equatorial region ~132 TECU. The increase may be caused by the influence of penetration electric fields and disturbance dynamo effects that redistribute plasma

from high to low mid latitude and possible traveling ionospheric disturbances (TIDs) triggered by the storm. The high latitude also increases modestly (~45 TECU), reflecting localized energy deposition from auroral processes (e.g, particle precipitation and joule heating). The lower magnitude of change compared to low latitudes reflects the spatial confinement of high latitude energy inputs.

The weakest TEC was observed on May 11. The day represents recovery phase with TEC values dropping significantly across all regions may be due to suppressed electric fields, thermo spheric cooling and plasma recombination processes. The TEC in equatorial region lowers to ~20 - 40 TECU which shows the ionosphere recovering rapidly as the storm time electric fields dissipate. The equatorial region shows a reduced diurnal pattern compared to May 9, reflecting the storm's residual impact. The night time TEC decreases to (~ 10 - 30 TECU). The absence of storm-induced plasma redistribution led to lower TEC levels compared to May 9-10, 2024. In high-latitude regions, TEC dropped to minimal levels (approximately 5-20 TECU), reflecting weakened auroral activity and reduced plasma content. On May 12, TEC stabilized, returning closer to pre-storm levels; however, slight elevations persisted in equatorial and mid-latitude regions due to the slow recovery of the thermosphere and ionosphere.

Additionally, storm-driven phenomena such as thermospheric winds, plasma drifts, and changes in neutral composition can create irregularities, redistributing electron density unevenly (Hargreaves, 1992; Kelly, 2009). This leads to a scenario where some areas experience sharp electron density gradients, while others display more subdued variations, reflecting the complex interplay of geomagnetic storm effects at low latitudes. Ionospheric irregularities in the global regions make ionospheric scintillations in the regions (Prikryl et al., 2010).

3.4. Scintillation Analysis and Statistical Correlations

To capture micro-scale diffractive impacts, high-rate amplitude scintillation (S4) indices shown in figure 8 were analyzed from four GNSS stations (*dwni, maci, nuel,* and *weip*). On May 10, prior to the primary main phase onset, a localized pre-storm enhancement occurred between 12:00 UT and 15:00 UT, pushing S4 values to a maximum range of 0.8–0.9 due to early solar wind interactions and pre-sunset plasma instabilities. During the primary main phase on May 11 (near the minimum Dst of −412 nT at 02:00 UT), the S4 index initially remained below 0.4 at these specific stations. This temporary low-scintillation response occurred because the stations were located in the daytime sector (Australia), suppressing the Rayleigh-Taylor instability required for

nocturnal EPB development. Following a localized dusk transition delay, scintillation intensities surged after 10:00 UT, peaking at a critical threshold of 0.9 by 20:00 UT across all four stations before dropping below 0.3 on May 12 as geomagnetic activity quieted down.

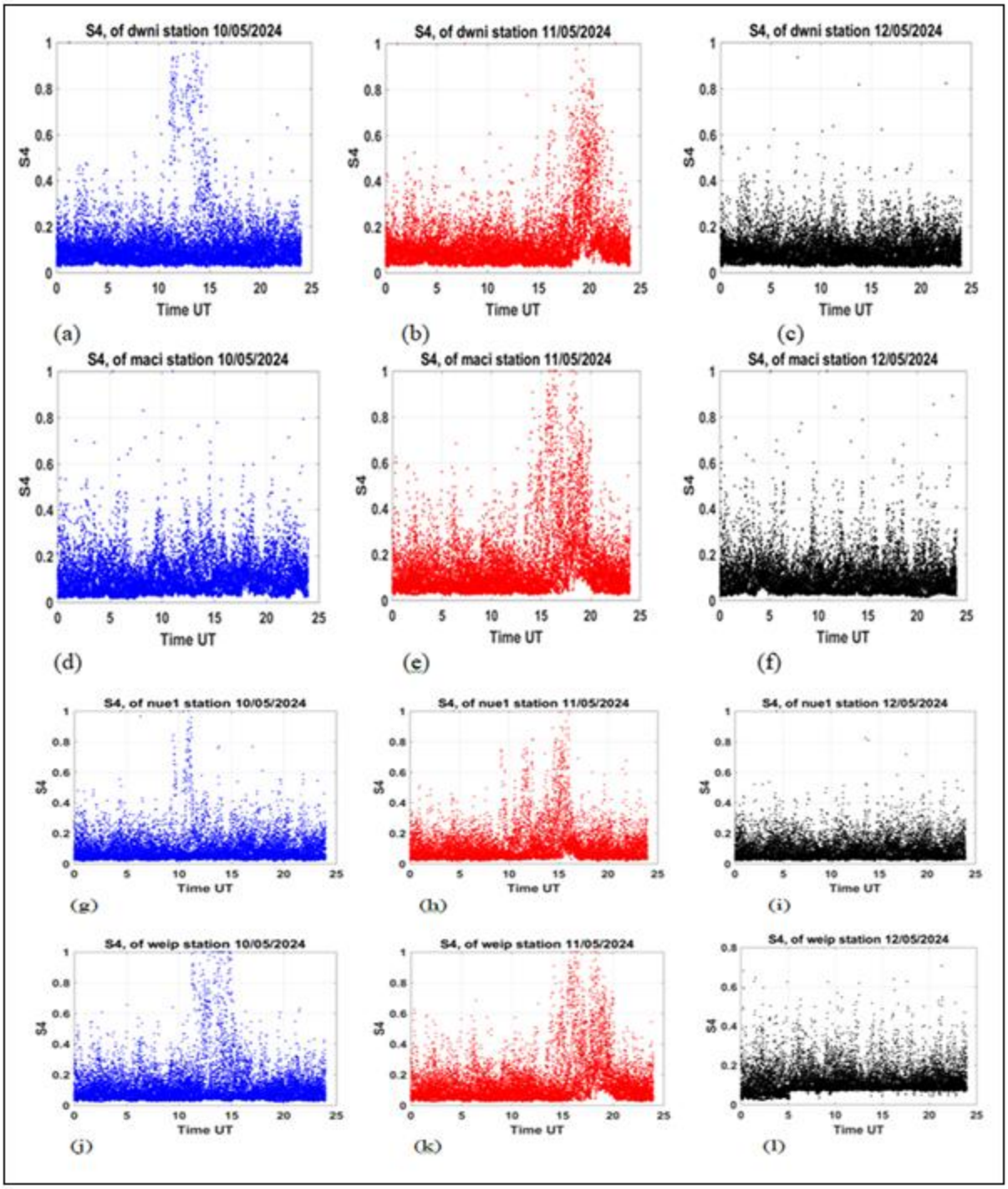


Figure 8. Sequential variations in mean ionospheric scintillation (S4) index observed at four selected GNSS stations during the May 10–12, 2024 period.

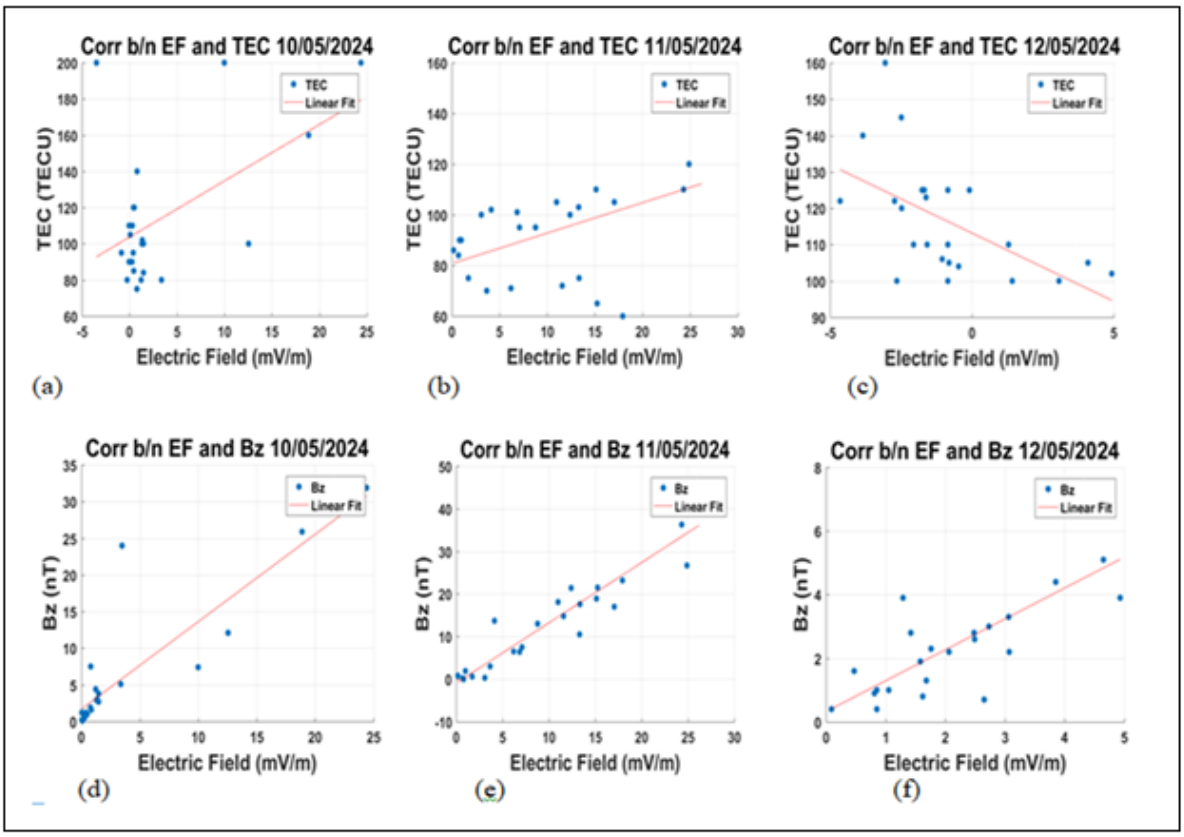


Figure 9. Statistical correlation of the ionospheric electric field with both Total Electron Content (TEC) and the interplanetary magnetic field component (IMF_{BZ}) for the period of May 10–12, 2024.

3.5. Correlation Between Electric Field, Total Electron Content and IMF-Bz

Statistical correlation analyses in figures 9(a-c) reveal the explicit electrodynamic coupling mechanisms operating throughout the event. Scatter plots matching the eastward ionospheric electric field (EF) and TEC demonstrated moderately strong positive linear relationships on May 10 (R=0.65) and May 11 (R=0.54), establishing that enhanced storm-time electric fields directly regulated plasma accumulation via vertical transport processes. Conversely, May 12 exhibited a prominent negative correlation (R=−0.59), reflecting slower plasma drifts that allowed localized accumulation over the equator while the primary electrojet driving subsided. Crucially, figures 9(d-f) shows correlation between the interplanetary magnetic field (IMF Bz) component and the induced eastward EF reached near-perfect linear dependencies of 0.87, 0.94, and 0.77 on May 10, 11, and 12, respectively. The peak coefficient of 0.94 during the main phase highlights that magnetospheric energy injection and direct PPEF modulation were the primary drivers behind the global ionospheric disturbances observed during this Solar Cycle 25 superstorm.

4. CONCLUSION

The extreme geomagnetic storm of May 10–12, 2024, generated severe, widespread disruptions across the global magnetosphere-ionosphere coupling system. Driven by an intense southward interplanetary magnetic field (IMF Bz=−46.5 nT) and exceptional plasma ram pressures (55.89 nPa), the storm drove the planetary indices to historic minimums (Dst=−412 nT) and maximums (Kp=9). The primary findings from this multi-instrument investigation demonstrate that:

- **Extreme EIA Poleward Expansion:** The combined influence of powerful daytime prompt penetration electric fields (PPEFs) and disturbed thermospheric winds forced the Equatorial Ionization Anomaly (EIA) crests to expand poleward up to an unprecedented $\pm 45^0$ magnetic latitude, with localized TEC accumulations exceeding 200 TECU.
- Multi-Scale Irregularity Alignment: High-resolution in-situ satellite tracks from the ESA Swarm constellation directly cross-validated ground-based observations, demonstrating that maximum electron density gradients ($\nabla Ne \approx 8$) and severe tracking indices (ROTI>0.8 TECU/min) matched the development of large-scale equatorial plasma bubbles and turbulent mid-latitude boundaries.
- **Severe Operational Scintillations:** High-rate ground receiver arrays registered severe amplitude scintillations ($S4 \approx 0.9$) across the post-sunset sectors, directly matching periods of tight statistical correlation ($R=0.94$) between IMF variations and the induced ionospheric electric fields.

These coordinated observations define the spatial boundaries of space weather anomalies during extreme solar maximum conditions. They provide high-resolution observational constraints necessary to adapt global communication infrastructures and multi-frequency GNSS tracking algorithms against severe ionospheric delays and trans-ionospheric signal degradation.

5. ACKNOWLEDGEMENTS

We gratefully acknowledge the use of data from various sources in this study. The OMNIWeb database provided essential solar wind and interplanetary magnetic field data, accessible through the NASA Goddard Space Flight Center's OMNIWeb platform (https://omniweb.gsfc.nasa.gov/form/dx4.html). The Global Positioning System (GPS) TEC data were obtained from the International GNSS Service (IGS) via the AGRID-2 project

(https://stdb2.isee.nagoya-u.ac.jp/GPS/shinbori/AGRID2/nc/index). Ionospheric and space weather data were sourced from the Australian SpaceWeather Services (SWS) (https://www.sws.bom.gov.au/world- Data-center). Swarm satellite data used in this research were accessed through the European Space Agency (ESA) Swarm Data Access portal. We also acknowledge the use of MATLAB software for processing and analyzing the data, which was instrumental in obtaining the results presented in this paper.

6. CONFLICT OF INTEREST

There is no conflict of interest.

7. REFERENCE

Afraimovich, E. L., Demyanov, V. V & Kondakova, T. N. 2002. Degradation of GPS performance in geomagnetically disturbed conditions. *arXiv e-prints physics,* 0211015, https://doi.org/10.48550/ arXiv.physics/0211015, arXiv:physics/0211015.

Akala, A. O., Oyedokun, O. J., Amaechi, P. O., Simi, K. G., Ogwala, A & Arowolo, O. A. 2021. Solar origins of August 26, 2018 geomagnetic storm: Responses of the interplanetary medium and equatorial/low-latitude ionosphere to the storm. *Space Weather*, **19**: e2021SW002734, https://doi.org/10.1029/2021SW002734.

Astafyeva, E., Bagiya, M. S., Förster, M & Nishitani, N. 2020**.** Unprecedented hemispheric asymmetries during a surprise ionospheric storm: A game of drivers. *Journal of Geophysical Research (Space Physics)*, **125(3)**: e2019JA027261, https://doi.org/10.1029/2019JA027261.

Baran, L. W., Ephishov I. I & Shagimuratov, I. I. S. 2001. Ionospheric total electron content behaviour during November 1997 storm. *Physics and Chemistry of the Earth*, **Part C 26**: 341–345, https://doi.org/10.1016/S1464-1917(01)00010-1.

Bauske, R & Prölss, G. W. 1998. Numerical simulation of long-duration positive ionospheric storm effects. *Advances in Space Research*, **22(1)**: 117–121, https://doi.org/10.1016/S0273-1177(97)01110-1.

Blagoveshchensky, D. V., Maltseva, O. A & Sergeeva, M. A. 2018. Impact of magnetic storms on the global TEC distribution. *Annales Geophysicae*, **36(4)**: 1057–1071, https://doi.org/10.5194/angeo-36-1057-2018.

Cherniak, I & Zakharenkova, I. 2015. Dependence of the high-latitude plasma irregularities on the auroral activity indices: A case study of 17 March 2015 geomagnetic storm. *Earth Planets Space,* **67(151)**: https://doi.org/10.1186/s40623-015-0316-x.

Dugassa, T., Mezgebe, N., Habarulema, J. B & Habyarimana, V. O. 2023. Ionospheric response to the 23–31 August 2018 geomagnetic storm in the Europe-African longitude sector using multi-instrument observations. *Advances in Space Research*, **71(3)**: 2269–2287, https://doi.org/10.1016/j.asr.2022.10.063.

Feng, J., Zhang, Y., Li, W., Han, B., Zhao, Z., Zhang, T & Huang, R. 2023. Analysis of ionospheric TEC response to solar and geomagnetic activities at different solar activity stages. *Advances in Space Research,* **71(5)**: 2225–2239, https://doi.org/10.1016/j.asr.2022.10.032.

Gonzalez, W. D., Joselyn, J. A., Kamide, Y., Kroehl, H. W., Rostoker, G., Tsurutani, B. T & Vasyliunas, V. M. 1994. What is a geomagnetic storm? *Journal of Geophysical Research (Space Physics)*, **99(A4)**: 5771–5792, https://doi.org/10.1029/93JA02867.

Gopalswamy, N. 2009. Halo coronal mass ejections and geomagnetic storms. *Earth, Planets and Space*, **61**: 595–597, https://doi.org/10.1186/BF03352930.

Hajra, R. Tsurutani, B. T. Lakhina, G. S & Lu, Q. D. 2024. Interplanetary Causes and Impacts of the 2024 May Super storm on the Geosphere. *Astrophysical Journal*, **974**: 264, https://doi.org/10.3847/1538-4357/ad7462arXiv:2408.14799.

Hargreaves, J. K. 1992, *The solar-terrestrial environment: An introductory to geospace the science of the terrestrial upper atmosphere, ionosphere and magnetosphere*. Cambridge University Press, New York, 434p.

Imam, R., Alfonsi, L., Spogli, L., Cesaroni, C & Dovis, F. 2024. On estimating the phase scintillation index using TEC provided by ISM and IGS 499 professional GNSS receivers and machine learning. *Advances in Space Research*, **73(7)**: 3753–3771, https://doi.org/ 10.1016/j.asr.2023.07.039.

Jacobsen, K., Linnea, S & Andalsvik, Y. 2016. Overview of the 2015 St. Patrick's Day storm and its consequences for RTK and PPP positioning in Norway. *Journal of Space Weather and Space Climate,* **6**: A9, https://doi.org/10.1051/swsc/2016004.

Jakowski, N., Schlüter, S & Sardon, E. 1999. Total electron content of the ionosphere during the geomagnetic storm on 10 January 1997. *Journal of Atmospheric and Solar-Terrestrial Physics*, **61**: 299-307, https://doi.org/ 10.1016/S1364-6826(98)00130-8.

Kelly, M. C. 2009. *The Earth's Ionosphere, plasma physics and electrodynamics*. 2nd edition, ISBN 978-0-12-088425-4, Academic Press (Elsevier), 576p.

Lanzerotti, L. J., Hunsucker, R. D & Hargreaves, J. K. 2004. The high latitude ionosphere and its effects on radio propagation. *Journal of Atmospheric and Solar-Terrestrial Physics*, **66**: 333–333, https://doi.org/10.1016/j.jastp.2003.10.008.

Li, G., Ning, B., Wang, C., Abdu, M. A., Otsuka, Y., Yamamoto, M & Wu, J. C. 2018. Storm-Enhanced Development of Posts unset Equatorial Plasma Bubbles Around the Meridian 1200E/600W on 7–8 September 2017. *Journal of Geophysical Research (Space Physics)*, **123**: 7985–7998, https://doi.org/10.1029/2018JA025871.

Lin, C. H., Richmond, A. D., Liu, J. Y., Yeh, H. C., Paxton, L. J., Lu, G., Tsai, H. F & Su, S. Y. 2005. Large-scale variations of the low-latitude ionosphere during the October-November 2003 superstorm: Observational results. *Journal of Geophysical Research (Space Physics)*, **110**: A09S28, https://doi.org/10.1029/2004JA010900.

Liu, Y., Li, Z & Wang, J. 2020. Studying the Ionospheric Responses Induced by a Geomagnetic Stormin September 2017 with Multiple Observations in America. In: *EGU General Assembly Conference Abstracts*, https://doi.org/ 10.5194/egusphere-egu2020-1906.

Maruyama, T & Nakamura, M. 2007. Conditions for intense ionospheric storms expanding to lower mid-latitudes. *Journal of Geophysical Research (Space Physics)*, **112(A5)**: A05310, https://doi.org/ 10.1029/2006JA012226.

Matsushita, S. 1959. A study of the morphology of ionospheric storms. *Journal of Geophysical Research*, **64(3)**: 305–321, https://doi.org/10.1029/JZ064i003p00305.

Nava, B., Rodríguez-Zuluaga, J., Alazo-Cuartas, K., Kashcheyev A., Migoya-Orué, Y., Radicella, S. M & Amory-Mazaudier, C. F. 2016. Middle- and low-latitude ionosphere response to 2015 St. Patrick's Day geomagnetic storm. *Journal of Geophysical Research (Space Physics)*, **121**: 3421-3438, https://doi.org/10.1002/2015JA022299.

Peng, Y., Scales, W. A., Hartinger, M. D & Xu, Z. C. 2021. Characterization of multi-scale ionospheric irregularities using ground-based and space-based GNSS observations. *Satellite Navigation*, **2**: 14, https://doi.org/10.1186/s43020-021-00047-x.

Pi, X., Mannucci, A. J., Lindqwister, U. J & Ho, C. M. 1997. Monitoring of global ionospheric irregularities using the Worldwide GPS Network. *Geophysical Research Letters*, **24(18)**: 2283–2286, https://doi.org/10.1029/97GL02273.

Prikryl, P. Jayachandran, P. T. Mushini, S. C. Pokhotelov, D. MacDougall, J. W. Donovan, E. Spanswick, E. St & Maurice, J. P. 2010. GPS TEC, scintillation and cycle slips observed at high latitudes during solar minimum. *Annales Geophysicae*, **28**: 1307–1316, https://doi.org/10.5194/angeo-28-1307-2010.

Sharma, S. K., Singh, A. K., Panda, S. K & Ahmed, S. S. 2020., The effect of geomagnetic storms on the total electron content over the low latitude Saudi Arab region: a focus on St. Patrick's Day storm. *Astrophysics and Space Science*, **365(2)**: 1–10, https://doi.org/10.1007/s10509-020-3747-1.

Tariku, Y. A. 2015. TEC prediction performance of the IRI-2012 model over Ethiopia during the rising phase of solar cycle 24 (2009–2011). 2015. *Earth, Planets and Space*, **67**: 140, https://doi.org/10.1186/s40623-015-0312-1.

Wan, X., Xiong, C., Gao, S., Huang, F., Liu, Y., Aa, E., Yin, F & Cai, H. 2021. The nighttime Ionospheric response and occurrence of equatorial plasma irregularities during geomagnetic storms: A case study. *Satellite Navigation,* **2(1)**: 23, https://doi.org/10.1186/s43020-021-00055-x.

Yin, P., Mitchell, C. N., Spencer, P. S. J & Foster, J. C. 2004. Ionospheric electron concentration imaging using GPS over the USA during the storm of July 2000. *Geophysical research letters*, **31**: L12806, https://doi.org/10.1029/2004GL019899.

Yuan, Y. Tscherning, C. C. Knudsen, P. Xu, G & Ou, J. 2008. The ionospheric eclipse factor method (IEFM) and its application to determining the ionospheric delay for GPS. *Journal of Geodesy,* 82: 1–8, https://doi.org/10.1007/s00190-007-0152-2.

Zakharenkova, I. E., Cherniak, I. V., Shagimuratov, I. I & Klimenko, M. V. 2018. Features of High-Latitude Ionospheric Irregularities Development as Revealed by Ground-Based GPS Observations, Satellite-Borne GPS Observations and Satellite In Situ Measurements over the Territory of Russia during the Geomagnetic Storm on March 17–18, 2018. *Geomagnetism and Aeronomy*, **58**: 70–82, https://doi.org/10.1134/S0016793217050176.

Zhang, S. R., Erickson P. J., Coster, A. J., Rideout, W., Vierinen, J., Jonah, O & Goncharenko, L. P. 2019. Subauroral and Polar Traveling Ionospheric Disturbances During the 7–9 September 2017 Storms. *Space Weather*, **17**: 1748–1764, https://doi.org/10.1029/2019SW002325.